Photovoltaic Sub-Module With Optical Sensor for Angular Measurements of Incident Light

João Paulo de Campos da Costa [ID], Rodrigo Henrique Gounella [ID], Wagner Benicio Bastos [ID], Elson Longo [ID], and João Paulo Carmo [ID]

Abstract—This paper presents a photovoltaic (PV) sub-module with an optical sensor for angular measurements of incident light. The optical sensor is a CMOS microdevice for accurate tracking of the solar incident angle for application on PV systems. This microdevice was designed in 0.7-μm CMOS and is composed by a matrix of photodiodes and the respective read-out circuits. A set of microstructures on metal with the widths of 5 and 10 μm was fabricated on the top of the photodiodes to allow the measuring of angles on a wide range of illuminations and for calibration purposes. The measurements done in the laboratory and in real-field open environments confirmed the suitability to track with good precision the maximum sun's incident angle in the range [0°, 180°], only limited by the servomotor to rotate the system. This PV sub-module measures 12 cm × 10 cm × 4 cm and presents a total power consumption of 265 mW, when supplied by 5 V. These features combined with the low cost of this PV sub-module bring excellent prospects for its installation on PV cells to achieve a maximum efficiency in the solar to electric energy conversion. To finish, this PV sub-module costs less than $130, opening good perspectives for its popularization.

Index Terms—Optical sensor, CMOS, angular measurement, photovoltaic cell, photovoltaic sub-module, solar tracking.

I. INTRODUCTION

IN RECENT years, our generation has been suffering from the scarcity of natural resources and climate changes. Thus, new research and investments in clean and renewable energy resources have been explored with the goal to modify and replace the energy matrix that is currently employed [1]. In this sense, it is necessary to develop low-cost devices with easy integration with photovoltaic cells to measure the angle of solar incidence in order to take full advantage of the power characteristics of these cells [2]–[9]. The integrated circuits based on CMOS technology offer a useful tool to produce low power optoelectronic microdevices [10], [11]. Normally, the CMOS microdevices use photodiodes to convert light into an electric current proportional to its intensity [12].
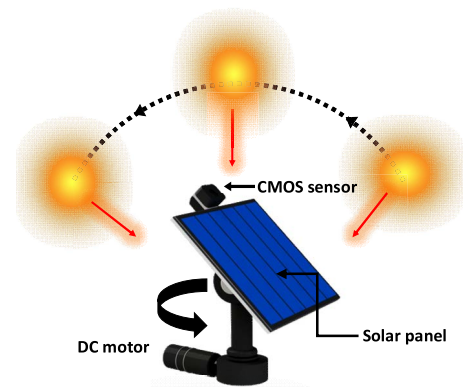
Fig. 1. Artwork representation of the solar tracking operation system using the PV sub-model with the CMOS sensor to detect the angle of incidence of light.

In this context, this paper presents a photovoltaic (PV) sub-module level for control systems, which uses an optical sensor based on CMOS to allow the precise measurement of the angle of solar light incidence. These measurements are then applied as an automatic tracker for photovoltaic cells, whose concept is illustrated in Fig. 1. Commercial sensors based on four quadrants for mounting on solar tracking systems have been proven to be very reliable with precisions of few milliradians [13]. The four quadrants approach was also achieved with photodiodes as a position sensor for providing a closed-loop control on mirrors positioning with a 20mrad of precision [14]. On a more microscale domain, the phenomena of grating coupling were used to modulate the coupling of the incident light into slab waveguides [15]. A low-cost solution based using the commercial Swiss sun tracker INTRA was provided at about 200USD [16]. However, all of these sun tracking solutions are bulky.

The PV sub-module presented in this paper is composed by an optical sensor that incorporates the photodiodes and the respective readout circuit in the same microdevice to provide accurate solar tracking with minimal weight, low power consumption and the possibility of large-scale production for installation on photovoltaic cells. This microdevice prototype was designed and fabricated in the 0.7μm CMOS process from the *on-semiconductor* [17]. The precision of the proposed PV sub-module is only limited by the mechanical positioning system, e.g., by the smallest step provided by the step motor.

This paper is organized as follows. Section II describes the relevant issues related to the design of the PV sub-module
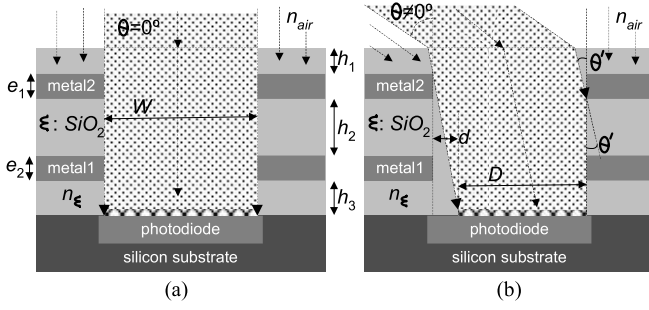
Fig. 2. Illustration showing the basic operation of the sensor for an incident light angle θ (a) equal and (b) different than 0°.

TABLE I
THICKNESSES OF THE LAYERS OF INTEREST [17], [21]

Layer	Thickness [µm]	Remark
e_1	0.71µm	Top layer or metal2 layer
e_2	0.66µm	Bottom layer or metal1 layer
h_1	1.00µm	Overlayer for protection against scratches
h_2	0.60µm	Via oxide layer or metal1-metal2 oxide layer
h_3	0.66µm	First oxide above the photodetector or metal1-active oxide layer

board. Section III presents all aspects related to the experiments and discussion of results. Finally, section IV discusses the cost comparison with other solutions and presents the final conclusions.

II. DESIGN

A. Concept

The operating principle of the developed sensor is based on the response generated on a photodiode, which is desired to be proportional to the angle of incidence of light. The transduction principle is based in the production of a generated photocurrent, whose intensity is proportional to the intensity of the impinging light [18], [19]. This intensity also depends to the angle of incidence. Fig. 2 illustrates the basic operation, where both the incidence area (chess-board-type shading) and the density of the impinging light in the photodiode decreases when the incidence angle θ increases. An array of photodiodes with and without metallic structures on top of the PN junctions was fabricated to allow the measuring under a wide range of intensities of illuminations and for self-calibration purposes. The angle detected by the photodiode depends on the refracted angle θ' in the dielectric layer, which in turns differs from the incident light angle θ. The value of θ' is given from the Snell's Law:

$$\theta = asin[sin(\theta') \cdot n_\varepsilon / n_{air}] \quad (1)$$

where n_ε and n_{air} are the refractive indexes of the dielectric layer and of the air, respectively [19]. The refractive index of the air is unitary, while the refractive index of the dielectric layer is the same of the silicon dioxide, e.g, $n_\varepsilon = 1.45$ [20].

As it can be observed in Fig. 2, the passage of light and the respective incidence in the photodiode's area is done on a way that the photocurrent produced by the photodiode is proportional to the angle θ'. Thus, the situation of maximum luminosity detected by the photodiode happens for $\theta' = 0°$. As it is also possible to observe in Fig. 2(b), the angle θ' can be determined as a function of the illuminated area of the photodiode represented by D. This angle is then given by:

$$\theta' = atan[d/(h_2 + h_3 + e_1 + e_2)] \quad (2)$$

where d represents the hidden area of the photodiode, h_i is the height of the dielectric layer $i = \{1, 2, 3\}$, e_1 the thickness of the top metal layer (metal2) and e_2 the thickness of

the bottom metal layer (metal1). Table I lists the values of these thicknesses and the respective physical meanings of the selected layers of the used CMOS technology [17]–[21]. The quantity D determines the amount of current detected. The maximum value of θ' was then calculated for two values of $W = d + D$, resulting equal to $\pm62.8°$ and $\pm75.6°$ for W respectively equal to $5\mu m$ and $10\mu m$.

B. Photodetectors

The photodetectors were designed and fabricated, using the same CMOS process of the readout and interface circuits to result on a single CMOS microdevice. A CMOS photodiode with a structure based on n^+/p-substrate junction was selected because it provides the best possible quantum efficiency in the spectral range between 350nm and 750nm. The response of these photodiodes covers the entire visible spectrum and thus, the majority of the spectral response of the mono-silicon solar cells. The produced photocurrent I_{ph} [A] is proportional to the intensity of the incident light [22]–[24], and is given by:

$$I_{ph} = e \times QE \times \lambda \times P_i/(hc) = e \times QE \times P_i/(h\nu) \quad (3)$$

where e [C] is the charge of the electron, λ [m] is the wavelength of the incident light, QE [%] is the quantum efficiency, P_i [W] is the incident optical power, h is the Plank's constant, and c [m·s^{-1}] is the velocity of light. The quantity $E_{ph} = hc/\lambda = h\nu$ [eV] is the energy of a photon and ν [Hz] is the frequency of the photons in the light. The quantum efficiency reflects the photon-sensitivity of a photodetector as a function of the wavelength of the impinging photons, which in formal terms is given by the ratio between the number of generated electrons N_e and the number of the incident photons N_{ph} in the photodetector. The quantum efficiency is then given by [22]–[24]:

$$QE = N_e/N_{ph} = (I_{ph}/e)/[P_i/(h\nu)] = R \times h\nu/e \quad (4)$$

where R is the responsivity of the photodetector measured in ampère per watt [A/W]. The responsivity is one of the most important photodetector's characteristics because it relates the generated photocurrent I_{ph} with the impinged optical power P_i, e.g., $R = I_{ph}/P_i$. For this reason, the responsivity is the physical characteristic to be obtained in the first place, after acquiring the photocurrents. Then, the quantum efficiency is calculated from the equation (4).

C. Readout Electronics

Fig. 3(a) shows the block diagram of the complete CMOS microdevice, whose operation is based on the charge
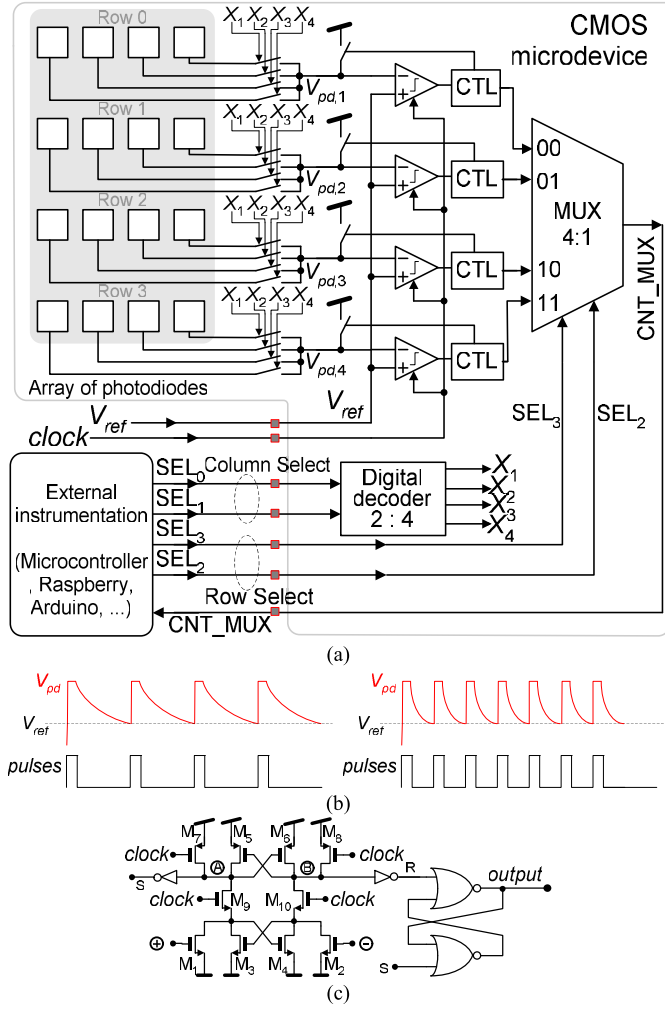
Fig. 3. (a) Block diagram of the CMOS microdevice, which comprises an array of 16 photodetectors and the readout electronics. (b) Shapes of V_{pd} and pulses for a fixed voltage V_{ref} for a given light intensity and for an higher light intensity. (c) The schematic of each comparator (regenerative feedback comparator).

balancing technique [25]. The developed microdevice is composed by a 4×4 array of photodiodes and the respective readout circuits. Only two photodiodes from the array was used in the sensor implementation. These photodiodes are located under two types of straps made of stacks of metal-2 (top metal) and metal-1 (bottom metal), measuring widths of $5\mu m$ (for the photodiode 1) and $10\mu m$ (for the photodiode 2) and separated by the same amount to measure the angles. Each readout circuit produces a pulsed signal, whose frequency depends on the intensity of light that impinges the surface of photodiode connected to the latter circuit. The individual readout circuit is composed by the photodiode itself, which works in charge balancing mode and is subjected to a periodic reset by the digital electronics (CTL blocks). The reset depends on the reference voltage V_{ref}. At the beginning of a cycle, the switch is closed and the supply voltage V_{dd} is applied in the photodiode. The junction capacitance of the photodiode is charged to V_{dd} and maintains this value with the switch closed. After the opening of the switch, a very small reverse current is established through the diode's junctions, discharging its

junction capacitance. This reverse current increase with the intensity of light (e.g., with P_i), therefore, V_{pd} decreases until crossing below V_{ref}. A new reset signal will be generated into the switch in the end of two clock cycles after V_{pd} have crossed below V_{ref}. Thus, the latter phenomena will repeat cyclically. It is also intuitive to deduce that increasing V_{ref} will increase f_{pulses} [Hz]. The calculation of $f_{pulses} = 1/T_{pulses}$ takes into account the period of pulses T_{pulses}, which is at least given by the sum of the three-time intervals t_1 [s], t_2 [s] and t_3 [s], e.g., $T_{pulses} \geq t_1 + t_2 + t_3$. The first time interval is the duration of two clock periods at the beginning of a cycle, e.g., $t_1 = 2/f_{CLK}$. The time interval t_2 is the time taken to discharge the junction capacitance of the photodiode C_j [F] from V_{dd} into V_{ref}, e.g.:

$$\Delta V = V_{dd} - V_{ref} = \frac{1}{C_j} \int_0^{t_2} I_{ph} dt \qquad (5)$$

resulting in $t_2 = C_j \cdot (V_{dd} - V_{ref})/I_{ph}$. Finally, t_3 is the time to allow the comparator to decide when V_{pd} is less than V_{ref} and to toggle the output, e.g., in the best scenario $t_3 = 2/f_{CLK}$. This means that the frequency of pulses is limited by:

$$f_{pulses} \leq 1/[C_j \cdot (V_{dd} - V_{ref})/(R \cdot P_i) + 4/f_{CLK}] \leq f_{CLK}/5 \quad (6)$$

whose value increases as a response to an increase either in the incident optical power either in the reference voltage or both. The power P_i can be measured by using a counter with a fixed time base T_{base} [s], whose counts are $N_{cnt} = T_{base} \cdot f_{pulses}$. Fig. 3(b) shows that with V_{ref} constant, the resulting value of the frequency increases if the intensity of light also increases.

It is also possible to observe in Fig. 3(a) that each row of photodetectors shares the same readout circuit with all simultaneously converting the light into pulsed signals. The signals SEL_0 and SEL_1 ensure that only a single photodiode of a given row connects into the readout circuit, e.g., only a single signal X_k is activated at a time. The signals SEL_2 and SEL_3 select the readout circuit (e.g., selects the line) whose output connects to CNT_MUX through the multiplexer.

Finally, Fig. 3(c) illustrates the schematic of a regenerative latch that was used in the implementation of the comparators [26]. This latch is composed by the pairs formed by M_3/M_4 and M_5/M_6, which are switched through their drains instead of their sources, in order to eliminate backgating effects and to promote faster regeneration. The regeneration is disabled (the pair M_3/M_4 is disconnected from the pair M_5/M_6 through M_9 and M_{10}) during the latch effect, where the clock signal is in the low state. This action forces the nodes A and B to the high state and the outputs of inverters (R and S) to the low state. The regenerative action of the latch causes an imbalance in the decision circuit forcing the outputs to take a state imposed by the inputs $+$ and $-$. Finally, a SR latch combines the outputs A and B signal in the *output* signal.

D. Photovoltaic (PV) Sub-Module

Fig. 4 shows a Computer Assisted Design (CAD) model of this photovoltaic (PV) sub-module board, which is composed by the optical sensor, a shield with connections to attach into an Arduino board, a Real Time Clock (RTC) module
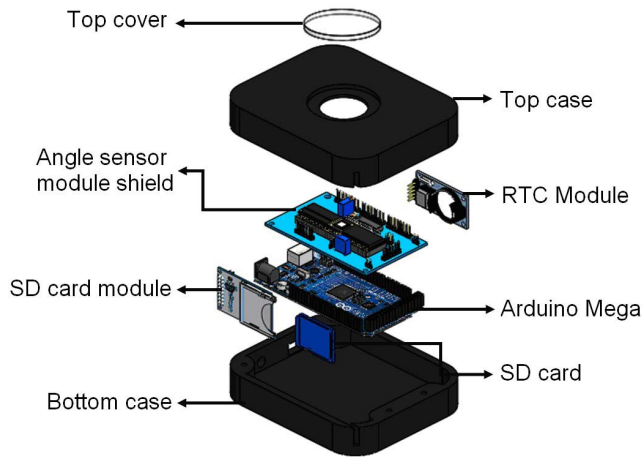
Fig. 4. Computer Assisted Design (CAD) model showing an exploded view of the components that compose the PV sub-module.
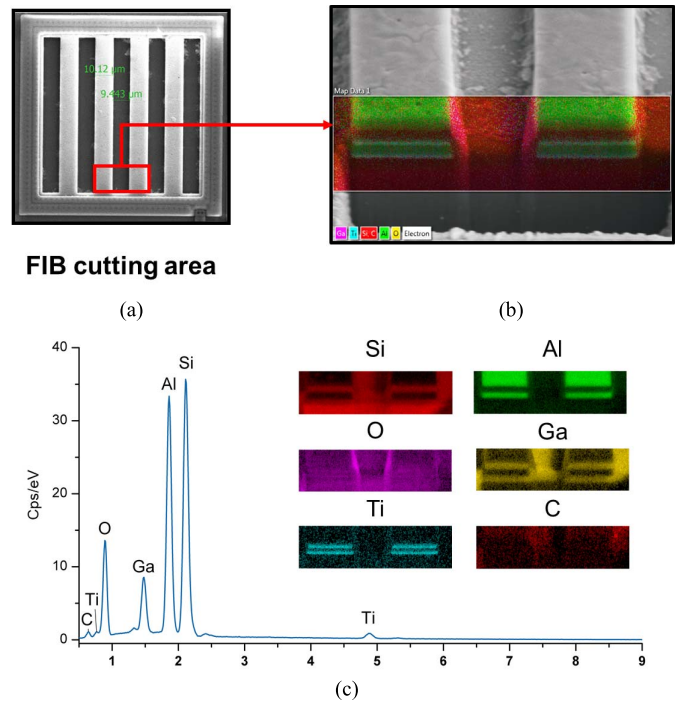

Fig. 5. For the characterization of the developed sensor: (a) SEM images of the photodetector used in this experiment; (b) the cross-section process made by FIB, showing the attenuator module on top of the photodiode; (c) the spectrum of the area analyzed from the sum of all X-ray collected data during the EDS acquisition, exhibiting the weight ratio of the constituent elements.

to provide information about the time and date, a module with a microSD card to store the acquired data for further processing, an optical attenuator to prevent the saturation of the optical sensor and a plastic case to protect the electronic circuits against the weather and dust particles. The plastic case was entirely printed by a 3D printer model GTMax®3D Core A1, using an ABS filament with a diameter of 1.75mm. The software Simplify3D® was also used to achieve the best possible performance and quality of printing with this filament. The Arduino shield is composed by the optical sensor for angular measurements, a clock generator (*clock*) based on a CA4093 gated oscillator, a potentiometer to trim the most suitable reference voltage V_{ref} and additional pins for future use by the PV sub-module. Each PV sub-module needs its own CMOS microdevice, but has the advantage to control simultaneously more than one PV panel.

III. EXPERIMENTAL RESULTS AND DISCUSSIONS

A. Optical Sensor for Angular Measurements Characterization

A FIB (Focused Ion Beam) FEI Nova 600 Nano Lab microscope with gallium ion sources was used in the characterization and cross-sectional experiments of the CMOS sensor. First, the CMOS sensor was fixed to the sample holder by carbon tape and inserted into the chamber. Then, the stage was tilted to an angle of 52° and placed at a working distance of 5mm for cross-sectional execution. A current of 170pA was used to carry out a cross section of $20\mu m$ of depth and a current of 86pA to polish the sample, in order to make the ionic milling at low voltage (5kV). Fig. 5(a) shows the scanning electron microscopy (SEM) images of the photodiode used on this experiment, which was selected for the beam cross section (gallium, Ga) FIB. Fig. 5(a) also shows the area selected for the cut. The SEM-EDS technique was used in the characterization of the sensor structure, more specifically, to determine the chemical composition (quantitative and qualitative) of a material. The EDS (Energy Dispersive X-ray Spectrometry) analysis was carried out using a X-Max

Silicon Drift Detector (SDD) from Oxford Instruments with 10kV of acceleration voltage, in order to collect the constituent elements of the CMOS sensor. Fig. 5(b) shows the SEM-EDS analysis that was performed in the selected cross-sectional area made by FIB, where it is possible to observe the uniformity of the deposition of the metallic layers made of Al and Ti (used as an adhesion layer), and the insulating layers composed by Si and O elements. Fig. 5(c) exhibit the spectrum of the analyzed area with EDS, which shows the weight ratio of the constituent elements. Fig. 5(c) also reveals the presence of Ga element, produced as a residue of the source of Ga-ions used in the etching process.

B. Characterization of Photodetectors

Both the responsivity R [A/W] and the quantum efficiency QE [%] of the photodiodes 1 and 2 (PD1 and PD2) were obtained experimentally at the laboratory. The experimental setup is composed by a 250W quartz tungsten halogen lamp from Oriel, a monochromator Newport model CornerStone 130 to sweep the wavelength from 405nm to 1000nm, an optical fiber Newport model Standard Grade FS Fiber Optic to couple the light into the photodetectors, a picoammeter Keithley 487 to measure the photocurrents of the photodiodes, and a commercial photodiode Hammamatsu with the reference S1336-5BQ to serve as reference to compensate the spectral signature of light at the output of monocromator. Normally, the responsivity is a parameter available in the datasheet of commercial photodetectors, which for the present case is given by $R_{commercial}$ [A/W].
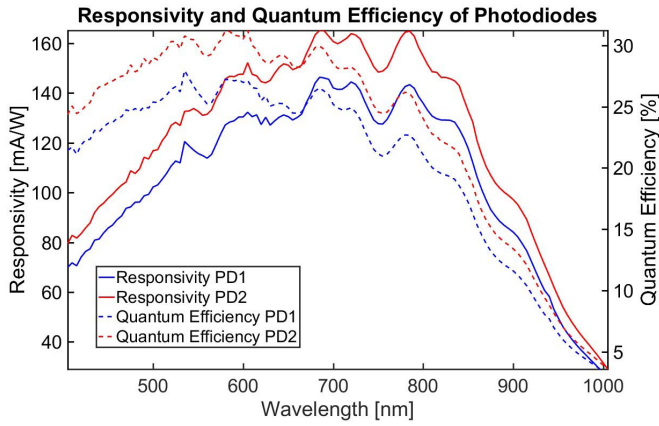
Fig. 6. Responsivities (continuous traces) and the quantum efficiencies (dashed traces) of the photodiodes 1 (in blue) and 2 (in red).

The photocurrents $I_{ph,1}$ and $I_{ph,2}$ of photodiodes 1 and 2 were acquired for each wavelength. The photocurrent of the commercial photodiode $I_{commercial}$ [A] was also acquired to compensate the spectral signature of light at the output of monocromator. The responsivity $R_{PD,i}$ [A/W] of each photodiode is then calculated according:

$$R_{PD,i} = f(\lambda) \times I_{ph,i} = (R_{commercial}/I_{commercial}) \times I_{ph,i} \quad (7)$$

where, $f(\lambda)$ is a function used in the spectral compensation. Fig. 6 shows the calculated responsivities (continuous traces) and the quantum efficiencies (dashed traces) of the photodiodes 1 (PD1 in blue) and 2 (PD2 in red). All the plots were overlapped for a better visualization.

C. Experimental Results at Laboratory

It was performed a set of preliminary tests in the laboratory to obtain the best parameters and frequency standards for detecting the solar incidence and the saturation of the photodiodes before conditioning the sensor to the final test of solar incidence. In this sequence, it was mounted a setup to determine the angle and its respective frequency generated by the incidence of light in the photodiode. Fig. 7(a) shows the configuration of this setup when assembled, which is composed by a rotating arm with a high-brightness LED located at the top and a servomotor in the lower end fixed into the optical table. The servomotor can rotate between 0° and 180°, while a potentiometer can be used to control the brightness of the LED. The CMOS sensor circuit was powered at $V_{dd} = 5$V. The voltage V_{ref} was derived from V_{dd} by a potentiometer settled to give 2V, while the CLK was settled at 50kHz through the CA4093 gated oscillator. The circuit output (CNT) was monitored via software with the collected data being collected and saved on a microSD card after each analysis. The sensors are read, and the data is collected for each individual position of the arm when performing the angular scan of a half revolution. The angular scan had an interval of 5° between each measurement. Fig. 7(b) shows a photograph of the setup used in the laboratory, and as it can be observed, the PV sub-module measures 12cm × 10cm × 4cm.
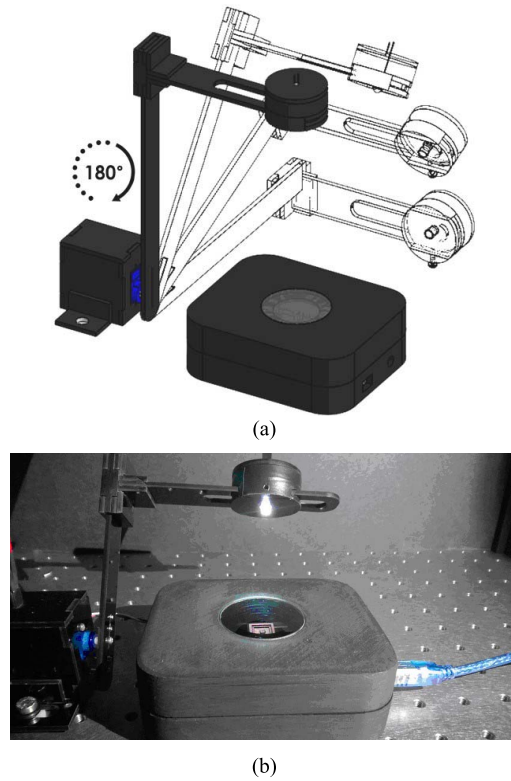

(a)

(b)

Fig. 7. For the experimental setup used in the laboratory: (a) an artwork showing a high brightness LED, a moving arm with a full rotation of 180°, and the PV sub-module; and (b) the respective photograph.
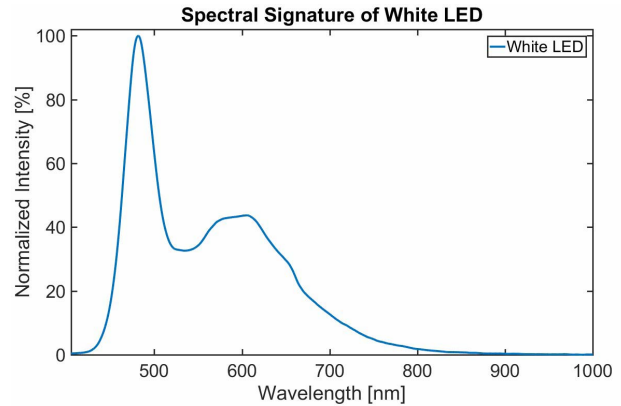

Fig. 8. Spectral signature of the white LED used in the laboratory tests.

A Vishay VLHW4101-YLWU white LED was used during the laboratory tests. Fig. 8 shows the spectral signature of this LED, which was acquired with a Thorlabs CCS200 portable spectrometer. This spectrometer has a USB interface to a personal computer and it can acquire the spectrums between 400nm and 1000nm, e.g., covering the entire visible region of the electromagnetic spectrum. The minimum and maximum strengths of the white LED were also measured, using a Thorlabs PMD120D power meter kit. This kit is composed by a PMD100D digital console to display the readings of the power densities (in W/cm²) and by a silicon detector S120C with a 400-1100nm wavelength range, 50nW-50mW power
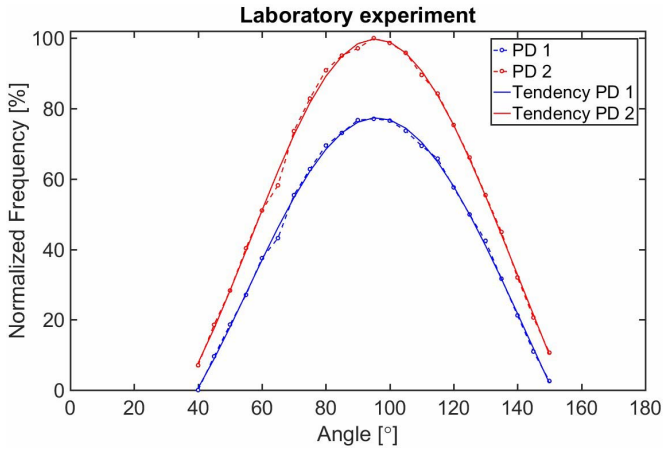
Fig. 9. Measured frequency that was obtained for the two photodiodes during the laboratory experiment. The frequency depends on the incidence angle of light in the two photodiodes. The tendency was also fitted to the measured points for better visualization and to take conclusions.

range, with a resolution of 1nm and a diameter of 9.5mm. The maximum strength of the white LED was measured under normal incidence (e.g., for a 90° rotation of the moving arm), resulting on $65\mu W/cm^2$. The minimum strength was measured for a 10° of the moving arm, resulting on $0.14\mu W/cm^2$.

Fig. 9 shows the measurement results obtained for the two photodiodes and as it can be observed, the frequency for both photodiodes approaches the maximum when the angle of incidence approaches 90°. In this way, it is possible to conclude that the sensor can determine the sun's position because this experience represents the LED as the Sun and the servo motor rotation as the rotation of the Earth around the Sun. The maximum frequency obtained in the experiment represents the position where the solar incidence is practically normal to the surface of Earth. Fig. 9 shows that the maximum frequency for both photodiodes is 95°, which is ideally expected, considering that the minimum variation of the servomotor in this experiment is 5° and at the same time, the error associated to this control is ±5°. The difference between the frequencies obtained during the measurements for each photodiode on equal circumstances demonstrates the sensitivity of the projected CMOS sensor, e.g., the frequency obtained with the photodiode 1 (in blue) is lower when compared to one obtained with the photodiode 2 (in red). This is explained by the fact that the photodiode 1 is designed to attenuate the light more effectively than the photodiode 2. Thus, it is possible to avoid possible monitoring problems of sunlight caused by saturation of the photodiode 2 on days with higher light intensity. On the other hand, the photodiode 1 could cause errors in tracking the solar incidence on days with lower light intensity, meaning the photodiode 2 to be more sensitive.

D. Solar Experiment

The PV sub-module with the sensor was installed and powered by a portable battery charger. The configuration used to track the solar position can be observed in Fig. 10. This setup contains a servomotor to tilt the case with all components of the sensor, sweeping the incidence angle from

Fig. 10. Experimental setup mounted on top of a roof, with a zoomed detail showing the photograph of the sensor installed on a servomotor and both powered by the battery charger powered by a photovoltaic cell.
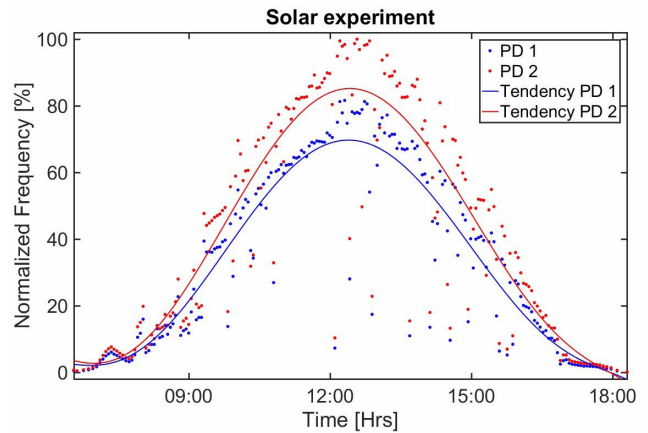

Fig. 11. Frequency as a function of time for the two photodiodes.

0° to 180° with a minimum variation of 5° (e.g., equal to the minimum variation of the previous configuration used in the laboratory). This motion is achieved by sweeping the pitch between −90° and +90°. It must be noted that the precision of this PV sub-module is only limited by the mechanical positioning system, e.g., by the smallest step provided by the step motor. Additionally, the sensor on this PV sub-module is sensitive to both the orthogonal directions, e.g., east-west and north-south. However, in order to sweep in the orthogonal direction, an additional servomotor is required to sweep the yaw from 0° to at least ±90°. A RTC module was added to perform the measurements of incidence angle in the open environment, in order to record the data during the measurements in the form of hours, minutes and seconds.

The difference from this system is that there is no rotating arm as in the laboratory experiment with the LED, so the whole case is rotated, and the frequency measurements of the photodiodes are obtained for all angles with an interval of approximately 2 minutes between each sequence from 0° to 180°. This data is stored on the microSD card. The experimental setup of the Fig. 10 (composed by the complete PV sub-module, powering and mechanical parts) is intended to give the best information about the rotation angle to prevent the bulky PV panel to be always rotating. This setup occupies
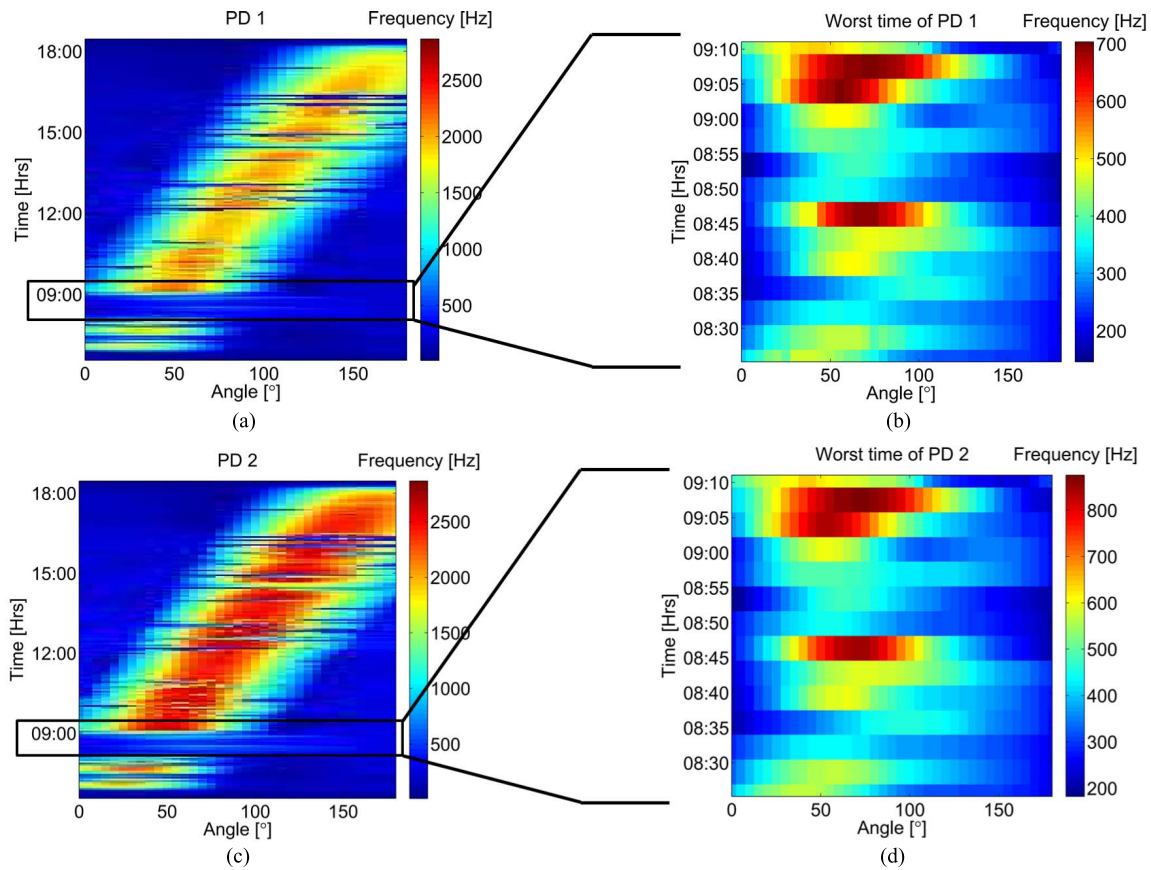
Fig. 12. Results obtained for the two photodiodes. (a) Frequencies measured over the analyzed period for photodiode 1. (b) Frequencies measured in the period where the fault occurs for the photodiode 1. (c) Frequencies measured over the period analyzed for photodiode 2. (d) Frequencies measured in the period where the fault occurs for the photodiode 2.

only 24cm × 10cm × 14cm and can be placed in any area with limited space and volume. For comparison purposes with the results obtained in the laboratory stage of this experiment, the data was collected when the system was positioned at 90°, during the all interval time in which the monitoring of solar incidence was performed. This time interval lasted for approximately 12 hours. The obtained results for the two photodiodes can be observed in Fig. 11, which shows that the frequency in both photodiodes increases and approaches the maximum when the day approaches midday. At this moment the solar incidence is practically perpendicular to the surface of Earth, demonstrating similarity with the laboratory experiment. In this experiment it is also possible to observe few points outside the curve in both photodiodes. This happens due to the coverage of the sun by the clouds, changing the luminous intensity.

Fig. 12 shows two-dimensional plots with the frequency measured for each angle between 0° and 180° over an analyzed period of approximately 12 hours. This different type of data was collected and analyzed for each photodiode 1 and 2 to demonstrate the ability of the system to determine the solar position throughout the day. Figs. 12(a) and (c) shows that the photodiodes were able to determine the highest incident solar incident angle during the entire period.

The maximum frequency, represented in red on the colored map of Fig. 12 changes according to the time of day and the

inclination angle of the sensor supplied by the servomotor. It is possible to verify that the sensitivity of the photodiode 1 is better than to the photodiode 2 in days with high light intensity, due to the attenuation of the metallic structures on top of this photodiode, while in the photodiode 2 it approaches the saturation point. Therefore, the photodiode 2 presents greater sensitivity for days with low light intensity. In general, the behavior of the two-dimensional plots in Fig. 12 is consistent with the behavior of the plots in Fig. 9. The apparent erratic behavior around the tendency represented by many dots randomly distributed in Fig. 11 is because these values were acquired on real-field conditions, e.g., with inconstant sun light due to the passage of clouds, birds and other environmental factors impossible to control. But despite the occurrence of these unpredictable factors and, as observed in Fig. 12, the PV sub-module can track with good precision the best angle of incidence.

Another relevant fact observed in Figs. 12(a) and (c) is a time interval between 8:25 hours and 9:10 hours, where the measured frequencies were very low about the rest of the analyzed period. The Figs. 12(b) and (d) are the magnifications of these ranges for photodiode 1 and photodiode 2 in Figs. 12(a) and (c), respectively. The reason for these failures in both graphs is the presence of clouds that attenuates the sunlight and causes deviations in the angle of incidence. However, with the sun's rays hidden, it is possible to verify by
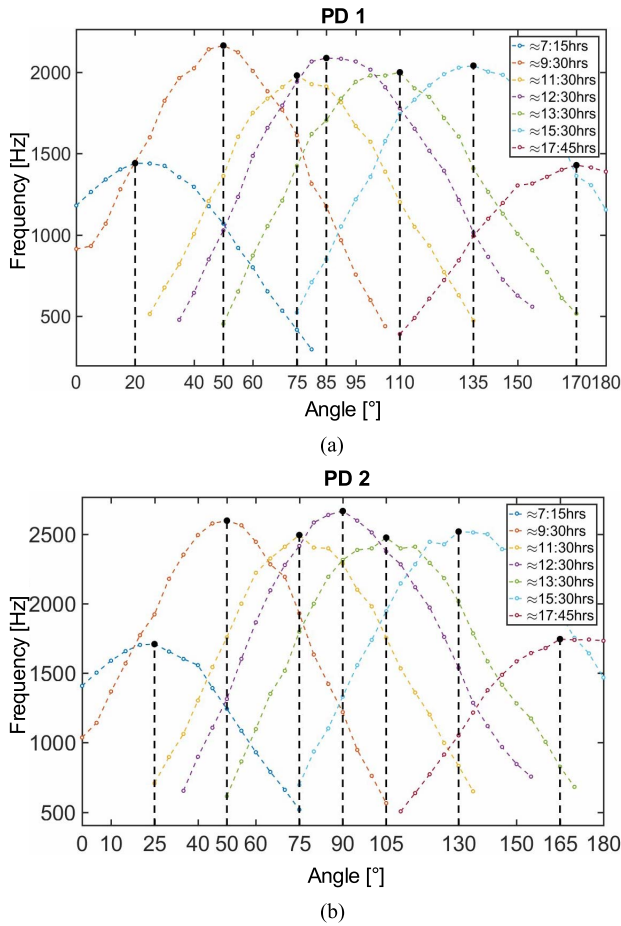
Fig. 13. Graphs for the seven periods during the day showing the exact angle where the frequency is maximum: (a) photodiode 1, and (b) photodiode 2.

TABLE II
COST OF THE PV SUB-MODULE

Real time clock module DS1307	$4.98
MicroSD card module	$6.45
Arduino Mega 2560 R3	$38.5
Discrete electronic components	$2.87
MicroSD card 4GB	$9,71
3D Printed box	$53.94
CMOS microdevice	$18,41
Total	**$129.10**

TABLE III
COSTS COMPARISON WITH OTHER SOLUTIONS

Sensor	Cost	Ref.	Remark
Array of photodiodes	$129.10	This work	Sensor and interface with RTC, SD card/module, arduino, etc.
4 quadrants	$542	[13]	Analog sensor (requires a tracker)
Thermopile	$200	[16]	Kipp & Zonen (commercial)
4 quadrants	$15000	[16]	INTRA Sun Tracker (commercial)
4 LDRs	$133	[28]	With two small PV cells, without communication interface
4 quadrants	$499.80	[29]	Thorlabs Inc. (commercial)
4 LDRs	$223.98	[30]	With a PV cell with Fresnel lens to concentrate the light, without communication interface
PV cell itself	$48	[31]	Without communication interface

IV. CONCLUSIONS

This paper presented a low-cost photovoltaic (PV) sub-module for angular measurements of incident light. Table II resumes the total cost of the major components. The cost calculation of the CMOS microdevice took into account the price per square mm of this technology and at the same time, that this price includes 30 dies [27]. In this context, Table III also provides a comparison of costs of this PV sub-module with similar solutions and applications found on academy and commercially available for better understanding purposes of the novelty of this work.

The developed PV sub-module was tested at the laboratory level and under real-field conditions. The results have proven possible to determine the angle of incidence of sunlight with greater intensity throughout the day, even with periods when the clouds have covered and attenuated the sunlight. Thus, this developed system can be applied in photovoltaic cells with automatic angle adjustment of the panel to obtain the maximum efficiency in the conversion of solar energy to electric energy.

the color map that the sensors are able to monitor the angle of incidence of the sun even if clouds cover it and, therefore, to determine the best position to increase the efficiency of the photovoltaic cells.

The significant points that cannot be perceived in the two-dimensional plots of Fig. 12 are the angles where exactly the maximum frequencies are located for each moment analyzed. For this, seven periods were separated during the time interval of the whole experiment, and with this, it was possible to construct the graphs presented in Figs. 13(a) and (b) for the photodiodes 1 and 2, respectively.

It was also measured the minimum threshold of sunshine for the PV sub-module in the solar experiment, using the power meter kit previously described. The measurement showed a minimum threshold of $2.65 \mu W/cm^2$.

In this way, it is possible to affirm that the system can determine the solar incidence angle with greater luminous intensity during the day. These points are signalized with more intense black spots and traced lines for better visualization of the maximum locations. It is also possible to observe in Fig. 13 that the maximums for the two photodiodes are not exactly located at the same angles, being explained once again by the fact that the servomotor has a variation of 5°. Therefore, the associated error is just ±5°.

REFERENCES

[1] N. Armaroli and V. Balzani, "The future of energy supply: Challenges and opportunities," *Angew. Chem. Int. Ed.*, vol. 46, nos. 1–2, pp. 52–66, Jan. 2007.

[2] C. Ranhotigamage and S. C. Mukhopadhyay, "Field trials and performance monitoring of distributed solar panels using a low-cost wireless sensors network for domestic applications," *IEEE Sensors J.*, vol. 11, no. 10, pp. 2583–2590, Oct. 2011.

[3] W. Y. Toh, Y. K. Tan, W. S. Koh, and L. Siek, "Autonomous wearable sensor nodes with flexible energy harvesting," *IEEE Sensors J.*, vol. 14, no. 7, pp. 2299–2306, Jul. 2014.

[4] T. V. Tran and W.-Y. Chung, "High-efficient energy harvester with flexible solar panel for a wearable sensor device," *IEEE Sensors J.*, vol. 16, no. 24, pp. 9021–9028, Dec. 2016.

[5] S.-H. Lee, "A passive transponder for visible light identification using a solar cell," *IEEE Sensors J.*, vol. 15, no. 10, pp. 5398–5403, Oct. 2015.

[6] L. C. Pita, S. E. S. Roman, J. M. Giron-Sierra, J. R. Barriga, P. D. de Vicente, and M. A. Jerez, "Getting more performance from INTA NanoSat-1B truncated pyramid sun sensors," *IEEE Sensors J.*, vol. 14, no. 6, pp. 1867–1877, Jun. 2014.

[7] S. Li and A. Pandharipande, "Networked illumination control with distributed light-harvesting wireless sensors," *IEEE Sensors J.*, vol. 15, no. 3, pp. 1662–1669, Mar. 2015.

[8] A. Díaz, R. Garrido, and J. J. Soto-Bernal, "A filtered sun sensor for solar tracking in HCPV and CSP systems," *IEEE Sensors J.*, vol. 19, no. 3, pp. 917–925, Feb. 2019.

[9] J. Barnes, C. Liu, and K. Ariyur, "A hemispherical sun sensor for orientation and geolocation," *IEEE Sensors J.*, vol. 14, no. 12, pp. 4423–4433, Dec. 2014.

[10] L. C. P. Gouveia and B. Choubey, "Advances on CMOS image sensors," *Sensor Rev.*, vol. 36, no. 3, pp. 231–239, Jun. 2016.

[11] C.-T. Chiang, J.-X. Lin, and L. Liu, "Design of a CMOS calibrated monolithic illumination meter for monitoring solar radiation of tomato crops," *IEEE Sensors J.*, vol. 15, no. 9, pp. 5285–5290, Sep. 2015.

[12] D. Fontani, P. Sansoni, F. Francini, D. Jafrancesco, L. Mercatelli, and E. Sani, "Pointing sensors and sun tracking techniques," *Int. J. Photoenergy*, vol. 2011, pp. 1–9, Mar. 2011.

[13] *ISSAX SUN SENSOR/Analog Sensor|Solar MEMS*. Accessed: Nov. 21, 2018. [Online]. Available: http://www.solar-mems.com/product/issax-sun-sensor-analog-sensor/

[14] A. Merlaud, M. De Mazière, C. Hermans, and A. Cornet, "Equations for solar tracking.," *Sensors*, vol. 12, no. 4, pp. 4074–4090, Mar. 2012.

[15] T. K. Saha, M. Lu, Z. Ma, and W. Zhou, "Design of an angle detector for laser beams based on grating coupling," *Micromachines*, vol. 3, no. 1, pp. 36–44, Feb. 2012.

[16] P. Roth, A. Georgiev, and H. Boudinov, "Cheap two axis sun following device," *Energy Convers. Manage.*, vol. 46, nos. 7–8, pp. 1179–1192, May 2005.

[17] *Europractice IC Service: Low Cost ASIC Prototyping (MPW) and Small-Medium Volume Production, 0.7 μm CMOS on-Semiconductor (Formerly AMI Semiconductor) 2 Metals/1-Poly Process, C07-D0.7 μm Option*. Accessed: Nov. 21, 2018. [Online]. Available: http://www.europractice-ic.com/technologies_AMIS_tech.php

[18] G. Minas, G. De Graaf, R. F. Wolffenbuttel, and J. H. Correia, "An MCM-based microsystem for colorimetric detection of biomolecules in biological fluids," *IEEE Sensors J.*, vol. 6, no. 4, pp. 1003–1009, Aug. 2006.

[19] P. Ortega *et al.*, "A miniaturized two axis sun sensor for attitude control of nano-satellites," *IEEE Sensors J.*, vol. 10, no. 10, pp. 1623–1632, Oct. 2010.

[20] M. F. Silva *et al.*, "NBI optical filters in minimally invasive medical devices," *IEEE J. Sel. Topics Quantum Electron.*, vol. 22, no. 4, Jul./Aug. 2016, Art. no. 6803307.

[21] R. G. Correia, S. Pimenta, and G. Minas, "CMOS integrated photodetectors and light-to-frequency converters for spectrophotometric measurements," *IEEE Sensors J.*, vol. 17, no. 11, pp. 3438–3445, Jun. 2017.

[22] H.-T. Wang and W. D. Leon-Salas, "An image sensor with joint sensing and energy harvesting functions," *IEEE Sensors J.*, vol. 15, no. 2, pp. 902–916, Feb. 2015.

[23] C.-C. Huang, J. K.-T. Huang, C.-W. Lee, and C. J. Lin, "A CMOS active pixel sensor with light intensity filtering characteristics for image thresholding application," *IEEE Sensors J.*, vol. 12, no. 5, pp. 1289–1293, May 2012.

[24] J. M. Gomes, J. H. Correia, and J. P. Carmo, "A low-cost flexible-platform (LCFP) for characterization of photodetectors," *Measurement*, vol. 61, pp. 206–215, Feb. 2015.

[25] J. H. Correia, G. de Graaf, M. Bartek, and R. F. Wolffenbuttel, "A CMOS optical microspectrometer with light-to-frequency converter, bus interface, and stray-light compensation," *IEEE Trans. Instrum. Meas.*, vol. 50, no. 6, pp. 1530–1537, Dec. 2001.

[26] R. Morais, A. Valente, C. Couto, and J. H. Correia, "A wireless RF CMOS mixed-signal interface for soil moisture measurements," *Sens. Actuators A, Phys.*, vol. 115, nos. 2–3, pp. 376–384, Sep. 2004.

[27] *Europractice IC Service: 2018 General MPW Runs Schedule and Prices*. Accessed: Nov. 21, 2018. [Online]. Available: http://www.europractice-ic.com/general_runschedule.php

[28] A. Acakpovi, N. Y. Asabere, and D. B. Sunny, "Low cost two-axis automatic solar tracking system," *Commun. Appl. Electron.*, vol. 3, no. 8, pp. 46–53, Dec. 2015.

[29] *Thorlabs—PDQ80A Quadrant Detector Sensor Head, 400 to 1050 nm*. Accessed: Nov. 21, 2018. [Online]. Available: https://www.thorlabs.com/thorproduct.cfm?partnumber=PDQ80A

[30] J.-N. Juang and R. Radharamanan, "Design of a solar tracking system for renewable energy," in *Proc. Zone 1 Conf. Amer. Soc. Eng. Educ.*, Apr. 2014, pp. 1–8.

[31] S. Kivrak, "Design of a low cost sun tracking controller system for photovoltaic panels," *J. Renew. Sustain. Energy*, vol. 5, no. 3, p. 033119, May 2013.

João Paulo de Campos da Costa was born in Brazil in 1991. He graduated in electrical engineering from the University of Araraquara in 2015 and received the M.Sc. degree in electrical engineering from the University of São Paulo, São Carlos, Brazil, in 2018, where he is currently pursuing the Ph.D. degree with the Telecommunications and Optics Group. He was an Electrical and Electronics Technician with the Industrial Learning Service–SENAI Henrique Lupo in 2009. He was a Researcher with the Center for the Development of Functional Materials (CDMF), where he has developed multifunctional materials through chemical and physical deposition processes for application in piezoelectric nanogenerators, gas sensors, varistors, and solar cells. He currently conducts scientific research on sensors and biosensors for application in laboratory diagnosis and develops an electron beam system for irradiation of semiconductor materials. He is a member of the CDMF/FAPESP Research Group.

Rodrigo Henrique Gounella was born in Brazil in 1991. He graduated in physics engineering from Federal University of São Carlos in 2016 and received the M.Sc. degree in electrical engineering from the Group of Metamaterials, Microwaves, and Optics telecommunications, University of São Paulo, São Carlos, in 2018, where he is currently pursuing the Ph.D. degree in electrical engineering. He developed a system for photodynamic therapy at the University of São Paulo. He was a Mechanical Technician with the Industrial Learning Service (SENAI) Antonio Adolpho Lobbe in 2007. He is currently conducting scientific research on RF transmitters for ISM 915-MHz and 2.4-GHz bands using TSMC 65-nm RF/MS CMOS technology.

Wagner Benicio Bastos was born in Brazil in 1973. He received the bachelor's degree in physics with a minor in electronic instrumentation in 2002, the M.Sc. degree in fluid dynamics simulation in 2005, and the Ph.D. degree in physics from the Physical Department, Federal University of São Carlos (UFSCar), Brazil, in 2011. He is a Developer of Instrumentation Systems for measurement and acquisition of data. He is also a Software Developer for scientific applications in new technologies, measurement, and data communication. He is a member of the CDMF/FAPESP Research Group and is currently conducting scientific research on ferroelectric, multiferroic, and semiconductor nanostructures using atomic force microscopy and piezoresponse microscopy at the LIEC Laboratories, Chemistry Department, UFSCar.

Elson Longo was born in Brazil in 1941. He graduated in chemistry from the Institute of Chemistry, São Paulo State University, Araraquara, in 1969, and received the M.Sc. degree in physics and the Ph.D. degree in chemistry from the Physics Institute, USP, São Carlos, in 1975 and 1984, respectively. He is currently the Emeritus Professor and the Chairman of the Department of Chemistry, Federal University of São Carlos, and maintains strong interchange with national and international research institutions in Spain, Portugal, France, USA, and Italy. He is also the Director of the Center for the Development of Functional Materials/FAPESP, where he is involved in the development of basic and technological research, teaching, and technology transfer to the private sector. He is a member of the International Academy of Ceramics (the World Academy of Ceramics), the Academy of Sciences of the State of São Paulo, and the Brazilian Academy of Sciences.

João Paulo Carmo was born in Portugal in 1970. He graduated in electrical engineering in 1993 and received the M.Sc. degree in electrical engineering from the University of Porto, Porto, Portugal, in 2002, and the Ph.D. degree in industrial electronics from the University of Minho, Guimarães, in 2007. He is currently a Professor with the University of São Paulo (USP), São Carlos, Brazil, where he is involved in the research on micro/nanofabrication technologies for mixed-mode/RF and optical microsystems, solid-state integrated sensors, microactuators, and micro/nanodevices for use in biomedical and industrial applications. He is also the Vice-Director of the Group of Metamaterials Microwaves and Optics, USP.